RSC Advances

PAPER

View Article Online
View Journal | View Issue

Cite this: *RSC Adv.*, 2020, **10**, 11244

Magnetic and structural properties of single-phase Gd^{3+}-substituted Co–Mg ferrite nanoparticles

El. Abouzir,[a] M. Elansary,[a] M. Belaiche *[a] and H. Jaziri[b]

Nanocrystalline Gd^{3+}-doped Co–Mg ferrite nanoparticles with the chemical formula $Co_{0.7}Mg_{0.3}Fe_{(2-x)}Gd_xO_4$ ($x = 0.02$) were prepared by coprecipitation for the first time. The properties of the nanoparticles were investigated by X-ray diffraction, confirming a single-phase, highly crystalline cubic spinel structure in the space group $Fd\bar{3}m$ and an average crystallite size of 54 nm. The Fourier-transform infrared spectrum showed two fundamental absorption bands in the wavenumber range of 437–748 cm^{-1} attributed to the stretching vibration of tetrahedral and octahedral sites in the spinel structure. Scanning electron microscopy analysis showed that the nanoparticles are different in shape and slightly agglomerated. Energy-dispersive X-ray spectroscopy demonstrated the purity of the nano-ferrite powder. Magnetic measurements revealed ferrimagnetic behavior at room and low temperatures with high coercivity and a high saturation magnetization of 95.68 emu g^{-1}, larger than that of pure bulk cobalt ferrite (80.8 emu g^{-1}). Only ferrite cobalt synthesized sonochemically has been reported to have a higher saturation magnetization (92.5 emu g^{-1}).

Received 26th February 2020
Accepted 3rd March 2020

DOI: 10.1039/d0ra01841d

rsc.li/rsc-advances

Introduction

Research in the past decades has suggested that nanotechnology will have crucial long-term effects on all industrial sectors. Compared to bulk materials, nanomaterials have increased reactivity due to their increased solubility and higher proportion of surface atoms. The magnetic, electrical, mechanical, and optical properties along with the specific electronic states of nanomaterials are also totally different from those of the equivalent bulk materials.

The specific properties of nanomaterials give them a variety of physical and chemical functionalities that are highly desirable for applications in numerous industrial sectors.[1–3] The unique structural characteristics, energetics, tailoring, and production strategies of nanostructures constitute the experimental and conceptual background for the field of nanoscience. The suitable control of nanostructure properties and activity can lead to new devices and technologies. The deviation of the properties of nanosized materials from those of the corresponding bulk materials is related to surface effects, which mainly depend upon the ratio of surface area to volume, the particle size, the chemical composition, and interactions between the particles. It should be noted that rapid developments in the field of nanotechnology have opened up vast possibilities for understanding and using magnetic materials.

In addition, many physical phenomena become more noticeable as the size of the system approaches the nanoscale. In recent years, a lot of work has been done on nanocrystalline materials because of their unusual and interesting properties compared to bulk materials.[4,5] Several research groups are investigating spinel oxide nanoparticles and particularly nano-ferrites because of their potential applications in magnetic devices, microwave technology, high-density magnetic recording media, cancer treatment, drug delivery systems, magnetic resonance imaging, and other fields.

The composition and synthetic method play crucial roles in determining the physical and chemical properties of ferrites. Several researchers have synthesized substituted nanoscale ferrites using the standard ceramic technique,[6] solid-state methods,[7] coprecipitation,[8,9] sol–gel methods,[10] molten salt routes,[11] electrodeposition,[12] and mecanosynthesis.[13] Other studies have focused on improving the physical properties of these nanomaterials. For example, Li *et al.* have shown that at the nanoscale, the shape, particle size, and cationic distribution play crucial roles in determining the physical properties of spinel ferrite.[14,15] They also demonstrated that the magneto-resistance of spinel ferrite decreases as the average grain size is reduced.[16,17]

Liu *et al.*[14] established a correlation between the coupling of the orbital angular momentum of electron spin in $CoFe_2O_4$ and the superparamagnetic properties of spinel ferrite nanoparticles ($MgFe_2O_4$) and deduced that due to the strong magnetic coupling of the Co^{2+} lattice sites, the blocking temperature of the $CoFe_2O_4$ nanoparticles was at least 150 °C

[a]*Nanomaterials and Nanotechnology Unit, E.N.S, Energy Research Centre, Faculty of Sciences, Mohammed V University, B.P. 5118 Takaddoum, Rabat, Morocco. E-mail: med.belaiche@um5.ac.ma*

[b]*Genetics and Molecular Biology, E.N.S, Mohammed V University, B.P. 5118 Takaddoum, Rabat, Morocco*

higher than that of $MgFe_2O_4$ nanoparticles of the same size. On the other hand, rare earth (RE) elements possess high magnetic moments, high magneto-crystalline anisotropy, and very high magnetostriction at low temperature due to the localized nature of 4f electrons. Thus, doping with small quantities of REs can improve the magnetic properties of nano-ferrites, particularly the magnetic coercivity, making them suitable for different applications (*e.g.*, the treatment of hyperthermia and other biomedical applications).[17,18] Although numerous nanometric cobalt ferrites have been produced by coprecipitation, few studies have been compared the cationic distributions and magnetic properties of RE-substituted cobalt powders. To our knowledge, the cation distributions and microstructural distributions of RE-doped Co–Mg nano-ferrites have not been reported. Despite the different synthetic techniques, no reports are available on gadolinium-substituted Co–Mg nano-ferrites. In this study, a coprecipitation method was used to synthesize $Co_{0.7}Mg_{0.3}Fe_{1.98}Gd_{0.02}O_4$ nano-ferrites. This method was chosen for its simplicity, short reaction time, low cost, and ability to product fine and homogeneous crystalline powders without any risk of contamination.

The objective of this work was to determine the effects of doping with Gd^{3+} on the structural, magnetic, and morphological properties of $Co_{0.7}Mg_{0.3}Fe_{(2-x)}Gd_xO_4$ ($x = 0.02$) nanoparticles prepared *via* coprecipitation. To the best of our knowledge, no similar work has been reported to date.

Characterization

The synthesized powder was characterized by X-ray diffraction (XRD; PANalytical PW3050/60) to determine the crystalline phase. The lattice parameters and crystallite sizes were calculated using Rietveld refinement and the Debye–Scherrer formula, respectively. Fourier-transform infrared (FTIR) spectra were recorded on a VERTEX 70 FTIR spectrometer over the range of 400–4000 cm^{-1}. Scanning electron microscopy (SEM; Quanta 200) coupled with energy-dispersive X-ray spectrometry (EDS) was used to determine the particle morphology and the chemical composition of the sample. Magnetic measurements were conducted using a Magnetic Property Measurement System (Quantum Design MPMS-XL-7AC SQUID) to study the magnetic behavior.

Experimental details

Gd^{3+}-doped Co–Mg ferrite with the chemical formula $Co_{0.7}Mg_{0.3}Fe_{2-x}Gd_xO_4$ ($x = 0.02$) was synthesized by chemical coprecipitation. First, $CoCl_2 \cdot 5H_2O$ (≥98% pure, Sigma-Aldrich), $FeCl_3$ (≥99.0% pure, Sigma-Aldrich), $Gd(NO_3)_3 \cdot 6H_2O$ (≥99.0% pure, Sigma-Aldrich), and $Mg(NO_3)_2$ (≥99.0% pure, Sigma-Aldrich) were dissolved stoichiometrically in deionized water. The mixture was stirred with a magnetic stirrer until the solution became homogeneous. The pH of the solution was adjusted to 12 *via* the dropwise addition of sodium hydroxide under constant stirring. The coprecipitated products were washed several times with deionized water to remove unwanted residual salts. The precipitates were then filtered and dried overnight in an oven at 100 °C. The resulting powders were calcined at 800 °C and 900 °C.

Results and discussion

XRD analysis

The powder XRD patterns of $Co_{0.7}Mg_{0.3}Fe_{1.98}Gd_{0.02}O_4$ calcined at 800 °C and 900 °C are shown in Fig. 1. The patterns of both samples indicate a highly pure, single-phase spinel crystal structure. The spectrum of the powder calcined at 800 °C has a parasitic peak corresponding to $GdFeO_3$ impurity, which is attributed to incomplete crystallization. In the spectrum of the powder calcined at 900 °C, the diffraction peaks located at 2θ values of 18.41°, 30.24°, 35.65°, 37.25°, 43.22°, 53.60°, and 57.16° correspond to the (111), (220), (311), (222), (400), (422), and (511) planes, respectively, which match exactly with the ICDD data card no #01-080-6487 (for $CoFe_2O_4$). These results confirm the formation of single-phase products. Thus, all dopants simply replaced the Co^{2+}–Fe^{3+} ions without distorting the cubic symmetry of the host cobalt ferrite, resulting in a single-phase cubic spinel structure (space group $Fd\bar{3}m$); no other impurities were detected in the high-purity cobalt ferrite both with and without gadolinium doping.

The Rietveld refinement of the average intensity profiles of nanocrystalline $CoFe_2O_4$ and $Co_{0.7}Mg_{0.3}Fe_{1.98}Gd_{0.02}O_4$ calcined at 900 °C was carried out using the program FULLPROF to determine the structural properties. The fitted patterns are in good agreement with the respective experimental data with good fitting parameters; the obtained lattice parameters a are 8.3784 and 8.3805 Å for $CoFe_2O_4$ and $Co_{0.7}Mg_{0.3}Fe_{1.98}Gd_{0.02}O_4$, respectively. All the peaks can be indexed to a spinel structure with space group $Fd\bar{3}m$. Fig. 2 and 3 show the typical refinements for $CoFe_2O_4$ and $Co_{0.7}Mg_{0.3}Fe_{1.98}Gd_{0.02}O_4$ after the final cycle of Rietveld refinement.

The average crystallite size D of each sample was determined from the full width at half maximum (FWHM) using the Debye–Scherrer formula:[19]

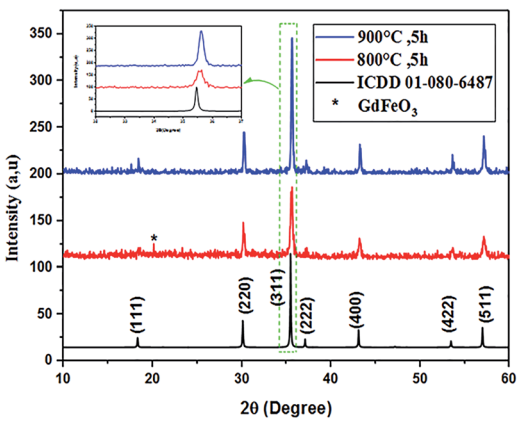

Fig. 1 XRD patterns of $Co_{0.7}Mg_{0.3}Fe_{1.98}Gd_{0.02}O_4$ calcined at 800 and 900 °C.

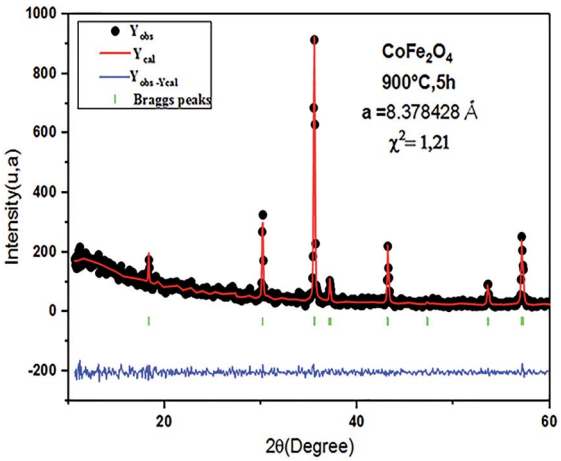

Fig. 2 Typical Rietveld-refined XRD pattern for the $CoFe_2O_4$ sample.

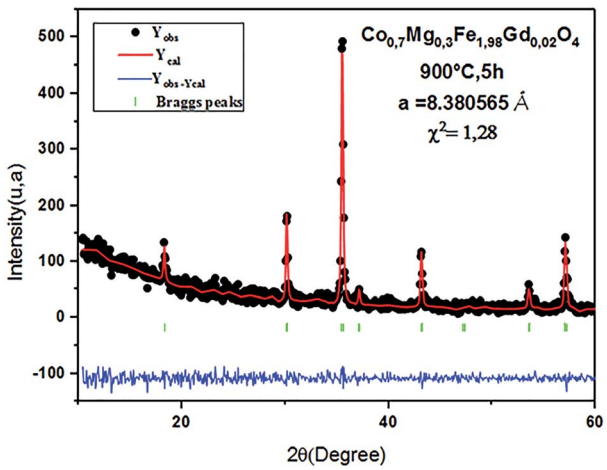

Fig. 3 Typical Rietveld-refined XRD pattern for the $Co_{0.7}Mg_{0.3}Fe_{1.98}Gd_{0.02}O_4$ sample.

$$D = \frac{0.90\lambda}{\beta \cos(\theta)}, \quad (1)$$

where λ is the wavelength of Cu(Kα) radiation, β is the FWHM, and θ is the Bragg diffraction angle.

The theoretical density $\rho_{X\text{-ray}}$ is determined by the following relation:[20]

$$\rho_{X\text{-ray}} = \frac{8M}{Na^3}, \quad (2)$$

where M is the molecular weight of the sample, N is Avogadro's number, and a is the lattice parameter.

The values of D and $\rho_{X\text{-ray}}$ determined from eqn (1) and (2) along with the a values calculated by Rietveld refinement are listed in Table 1.

The lattice parameter a = 8.3805 Å for $Co_{0.7}Mg_{0.3}Fe_{1.98}Gd_{0.02}O_4$ was larger than that of $CoFe_2O_4$ (a = 8.3784 Å). This can be attributed to the larger ionic radii of Gd^{3+} (0.094 nm) and Co^{2+} (0.074 nm) at the octahedral site compared to the radii of Fe^{3+} (0.067 nm) and Mg^{2+} (0.072 nm), which resulted in an overall expansion of the lattice.

As shown in Table 1, The calculated value of the average crystallite size (D), of the doped sample $Co_{0.7}Mg_{0.3}Fe_{1.98}Gd_{0.02}O_4$ is smaller than that of the undoped cobalt ferrite $CoFe_2O_4$, a result that is similar to those reported for RE-doped ferrites. Indeed, by comparing our results with those found in the literature, we noticed that we observed similar structural behavior with that described in previous work, in terms of an increase in the lattice parameter and decrease in the average crystallite size, but totally different magnetic behavior.[21–24] Indeed, in the case of the two substitutions by magnesium and gadolinium, the saturation magnetization and coercivity decrease, whereas in our case the saturation magnetization and coercivity increase drastically despite having been doped with a low concentration of gadolinium. This phenomenon will be better elucidated later when discussing the magnetic properties.

From a structural point of view, this situation can result from the fact that the higher binding energy of Gd^{3+}–O^{2-} compared to Fe^{3+}–O^{2-}. In fact, a large amount of energy is necessary to replace Fe^{3+} with Gd^{3+}. As a result, Gd^{3+}-substituted ferrites have higher thermal stability than pure cobalt ferrites. The smaller crystallite size may also be related to the pressure created by the larger crystals of Gd^{3+} ions (large ionic rays) on the grain boundaries.[25,26]

The calculated $\rho_{X\text{-ray}}$ value of $Co_{0.7}Mg_{0.3}Fe_{1.98}Gd_{0.02}O_4$ is small compared to that of pure $CoFe_2O_4$. This can be explained by the decrease in molecular weight upon doping with Gd^{3+} and Mg^{2+}. The relative molecular weight decreases as more Co^{2+} is replaced by Mg^{2+} since the atomic weight of Co^{2+} is greater than that of Mg. In addition, the atomic percentage of Gd^{3+} in this compound is much smaller than that of Mg^{2+}.

Table 1 Crystallite size (D), lattice parameter (a), and X-ray density ($\rho_{X\text{-ray}}$) values for $CoFe_2O_4$ and $Co_{0.7}Mg_{0.3}Fe_{1.98}Gd_{0.02}O_4$

Sample	Lattice parameter a (Å)	Average crystallite size D (nm)	Theoretical density $\rho_{X\text{-ray}}$ (g cm^{-3})	Reference
$CoFe_2O_4$	8.378	81	5.299	Present work
$Co_{0.7}Mg_{0.3}Fe_{1.98}Gd_{0.02}O_4$	8.380	54	5.295	
$CoFe_2O_4$	8.355	56	5.347	21
$Co_{0.7}Mg_{0.3}Fe_2O_4$	8.387	48	5.050	
$CoFe_2O_4$	8.354	55	5.346	22
$CoFe_{1.96}Gd_{0.04}O_4$	8.397	34	5.353	

Bulk cobalt ferrite has an inverse spinel structure that shifts to a partially inverted structure in the case of nano-ferrites. In the inverse spinel, eight of the tetrahedral sites are occupied by Fe^{3+}, and half of the octahedral sites are occupied by Co^{2+} and Fe^{3+}. When the size is reduced to the nanoscale, some of the Co^{2+} ions at the octahedral site migrate to the tetrahedral site, leading to a partially inverted structure. Cobalt ferrite belongs to space group $Fd\bar{3}m$, and the lattice parameter is typically close to 8.39 Å.[27]

In the literature, $MgFe_2O_4$ has been reported to have a partially inverted spinel ferrite structure.[28] The distribution of metal ions in $MgFe_2O_4$ is given as $(Mg_{1-x}Fe_x)[Mg_xFe_{2-x}]O_4$, where the parenthesis and square brackets denote cation sites of tetrahedral (A-sites) and octahedral [B-sites] coordination, respectively.[29]

Studies have been conducted on the effects of the substitution of Co by Mg on the physicochemical properties of cobalt ferrite and *vice versa*. Several studies have been reported on the effect of metal ion substitution on the structure and magnetic properties of $MgFe_2O_4$. The main objective of these studies was to synthesize pure nanocrystalline powders with the general formula $Mg_xCo_{1-x}Fe_2O_4$ ($0.00 \leq x \leq 1.00$).

The structural, morphological, electrical, dielectric, and magnetic properties of Co–Mg ferrite have been studied[30] while continuing to verify and improve the quality of ferrite for various applications. Several experimental techniques have been used to evaluate the degree of inversion in these spinel systems, including X-ray absorption, neutron and X-ray diffraction, and Raman and Mössbauer spectroscopy. However, these methods alone cannot determine the cation distribution in $Co_xMg_{1-x}Fe_2O_4$ because they only target iron ions (reported results are summarized in Table 2). Therefore, it is interesting to study the properties of Co–Mg ferrite nanoparticles doped with gadolinium because the expected improvement in the structure can lead to the improvement of the magnetic properties.

According to the literature and in the light of the considerations mentioned above, the suggested cation distribution for the $Co_{0.7}Mg_{0.3}Fe_{1.98}Gd_{0.02}O_4$ samples in this study can be written as

$$[Mg_\delta Fe_{1-\delta}]^A[Co_{1-\delta-\gamma}Mg_\gamma Fe_{0.98+\delta}Gd_{0.02}]^B O_4,$$

where γ is the concentration of Mg^{2+} ions, and δ is the degree of inversion represented by the percentages of Mg^{2+} and Fe^{3+} at tetrahedral and octahedral sites.

The mean ionic radii of ions at the tetrahedral site r_{tet} and octahedral site r_{oct} can be described in terms of their concentrations as

$$r_{tet} = [\delta r_{Mg^{2+}} + (1 - \delta) r_{Fe^{3+}}], \quad (3)$$

and

$$r_{oct} = \frac{1}{2}\left[(1 - \delta - \gamma) r_{Co^{2+}} + \gamma r_{Mg^{2+}} + (0.98 + \delta) r_{Fe^{3+}} + 0.02 r_{Gd^{3+}}\right], \quad (4)$$

where $r_{Fe^{3+}}$, $r_{Co^{2+}}$, $r_{Gd^{3+}}$, and $r_{Mg^{2+}}$ are the radii of Fe^{3+}, Co^{2+}, Gd^{3+}, and Mg^{2+} ions, respectively.

The lattice parameter can be calculated theoretically by the following equation:[38]

$$a_{th} = \frac{8}{3\sqrt{3}}\left[(r_A + R_O) + \sqrt{3}\,(r_B + R_O)\right], \quad (5)$$

where R_O is the radius of oxygen ion ($R_O = 1.32$ Å), and r_A and r_B are the radii of the tetrahedral and octahedral sites, respectively.

A mathematical model based on the formula proposed for cation distribution was constructed to search for the best match between the theoretical and experimental values of the lattice constant for the sample by optimizing the values of the parameters δ and γ over the tetrahedral and octahedral sites; the obtained cation distribution is shown in Table 3.

The results obtained from the proposed model are in very good agreement with those obtained experimentally by Nakagomi *et al.*[36] using Mössbauer and Raman spectroscopy.

From the results reported previously, it is clear that the tetrahedral site A is mainly occupied by Fe^{3+} ions and a low percentage of Mg^{2+} ions, while the octahedral site B is occupied by Fe^{3+}, Gd^{3+}, Co^{2+}, and Mg^{2+} ions, in good agreement with other results obtained by different experimental methods (Table 2).

The spinel structure has a cubic arrangement of O^{2-} ions (fcc); each unit cell contains eight AB_2O_4 units with the space group $Fd\bar{3}m$. The atom locations in the spinel depend on the choice of the origin in the space group $Fd\bar{3}m$. The conventional choices for the origin in the cells of the spinel unit are either a cation site A with $\bar{4}3m$ symmetry or an octahedral vacancy with $\bar{3}m$ symmetry.[39]

If the cation site A with $\bar{4}3m$ symmetry is taken as the origin, the oxygen position parameter or the anionic parameter u, which is the distance between the oxygen ion and the face of the

Table 2 Cation distributions found in the literature

	Site A	Site B	Method	Reference
Coprecipitation	$[Mg_{0.1}Fe_{0.9}]$	$[Co_{0.7}Mg_{0.2}Fe_{1.08}Gd_{0.02}]$	Mathematical model	Present work
	$[Mg_{0.1}Fe_{0.9}]$	$[Mg_{0.4}Co_{0.5}Fe_{1.1}]$	XRD	31
	$[Co_{0.31}Fe_{0.69}]$	$[Co_{0.69}Gd_{0.03}Fe_{1.28}]$	Rietveld analysis	32
Sol–gel	$[Co_{0.106}Mg_{0.049}Fe_{0.85}]$	$[Mg_{0.007}Co_{0.85}Fe_{1.2}]$	Mössbauer spectroscopy	33
	$[Mg_{0.51}Fe_{0.49}]$	$[Mg_{0.29}Co_{0.2}Fe_{1.51}]$	Mathematical model	34
	$[Mg_{0.159}Fe_{0.841}]$	$[Mg_{0.841}Fe_{1.159}]$	Rietveld analysis	35
	$[Mg_{0.15}Fe_{0.85}]$	$[Mg_{0.86}Fe_{1.15}]$	Mössbauer spectroscopy	36
	$[Mg_{0.14}Fe_{0.86}]$	$[Mg_{0.87}Fe_{1.13}]$	Raman spectroscopy	
Ceramic method	$[Zn_{0.5}Mg_{0.08}Fe_{0.62}]$	$[Mg_{0.62}Fe_{1.38}]$	Mössbauer spectroscopy	37

Table 3 Cation distribution of $Co_{0.7}Mg_{0.3}Fe_{1.98}Gd_{0.02}O_4$

				Cation distribution	
a_{exp}	a_{th}	r_A	r_B	A-site	B-site
8.3805	8.38016	0.6750	0.7022	$Mg_{0.1}Fe_{0.9}$	$Co_{0.7}Mg_{0.2}Fe_{1.08}Gd_{0.02}$

edge along the cube diagonal of the spinel lattice, is calculated by[40]

$$u(\bar{4}3m) = \frac{(r_A + R_O)}{a_{exp}\sqrt{3}} + \frac{1}{4}, \quad (6)$$

where r_A is the ionic radius of the A-site, and R_O is the ionic radius of oxygen ion.

The calculated values of $u(\bar{4}3m)$ are 0.37886 and 0.3874 Å for the $CoFe_2O_4$ and $Co_{0.7}Mg_{0.3}Fe_{1.98}Gd_{0.02}O_4$ samples, respectively. The decrease in the oxygen positional parameter can be explained by the occupation of the Gd^{3+} only the octahedral sites but Mg^{2+} ions at the octahedral and tetrahedral sites. Consequently, the distance between the A and O^{2-} ions decreased, while that between B and O^{2-} increased.[41]

FTIR spectra

FTIR spectroscopy makes it possible to predict the presence of the different bonds in a crystal. The FTIR spectra of the $CoFe_2O_4$ and $Co_{0.7}Mg_{0.3}Fe_{1.98}Gd_{0.02}O_4$ samples were recorded at room temperature in the wavenumber range of 400–4000 cm^{-1} (Fig. 4).

The positions of the vibrational bands of $CoFe_2O_4$ and $Co_{0.7}Mg_{0.3}Fe_{1.98}Gd_{0.02}O_4$ are given in Table 4. For spinel ferrites, the vibrational band at around 750–850 cm^{-1} corresponds to the stretching vibration of the tetrahedral site, while the vibrational band at around 400–500 cm^{-1} corresponds to the stretching vibration of the octahedral site.[33,42]

Table 4 FTIR vibrational bands of $CoFe_2O_4$ and $Co_{0.7}Mg_{0.3}Fe_{1.98}Gd_{0.02}O_4$

	ν_1 (cm^{-1})	ν_2 (cm^{-1})	ν_3 (cm^{-1})
$CoFe_2O_4$	437.0807	779.7678	—
$Co_{0.7}Mg_{0.3}Fe_{1.98}Gd_{0.02}O_4$	445.28849	812.0047	1165.5477

Table 4 indicates that the vibrational spectra consist of two main bands (ν_1 = 437.0807 cm^{-1} and ν_2 = 779.7678 cm^{-1}) for $CoFe_2O_4$ and three bands (ν_1 = 445.28849 cm^{-1}, ν_2 = 812.0047 cm^{-1}, and ν_3 = 1165.5477 cm^{-1}) for

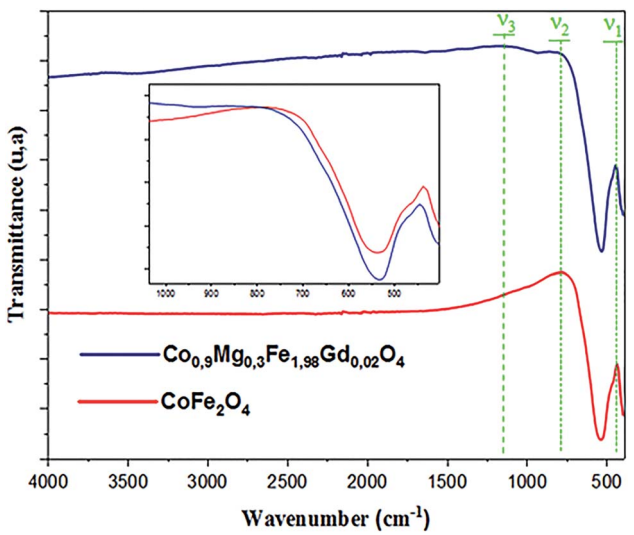

Fig. 4 FTIR spectra of samples $Co_{0.7}Mg_{0.3}Fe_{1.98}Gd_{0.02}O_4$ and $CoFe_2O_4$.

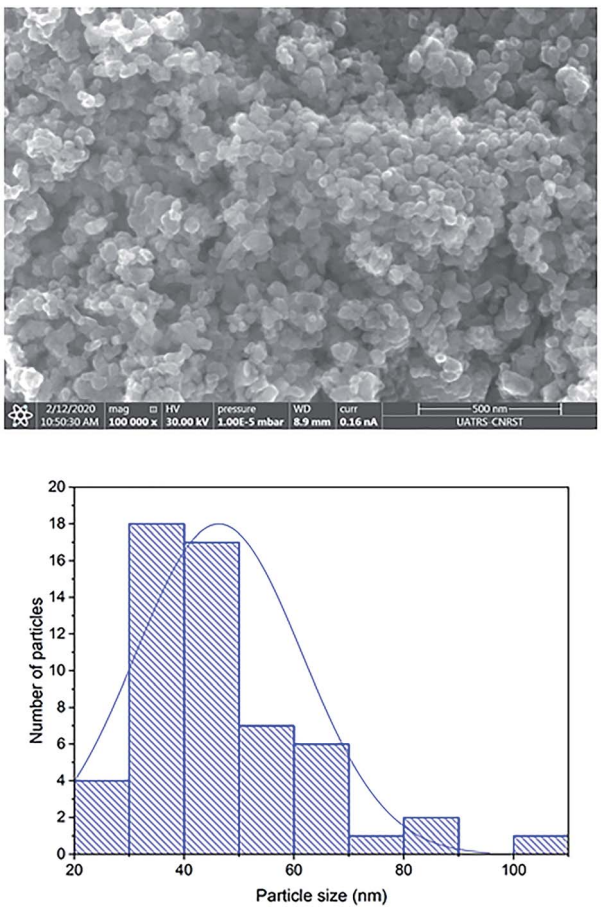

Fig. 5 SEM image of $Co_{0.7}Mg_{0.3}Fe_{1.98}Gd_{0.02}O_4$ nanoparticles and the corresponding particle size distribution.

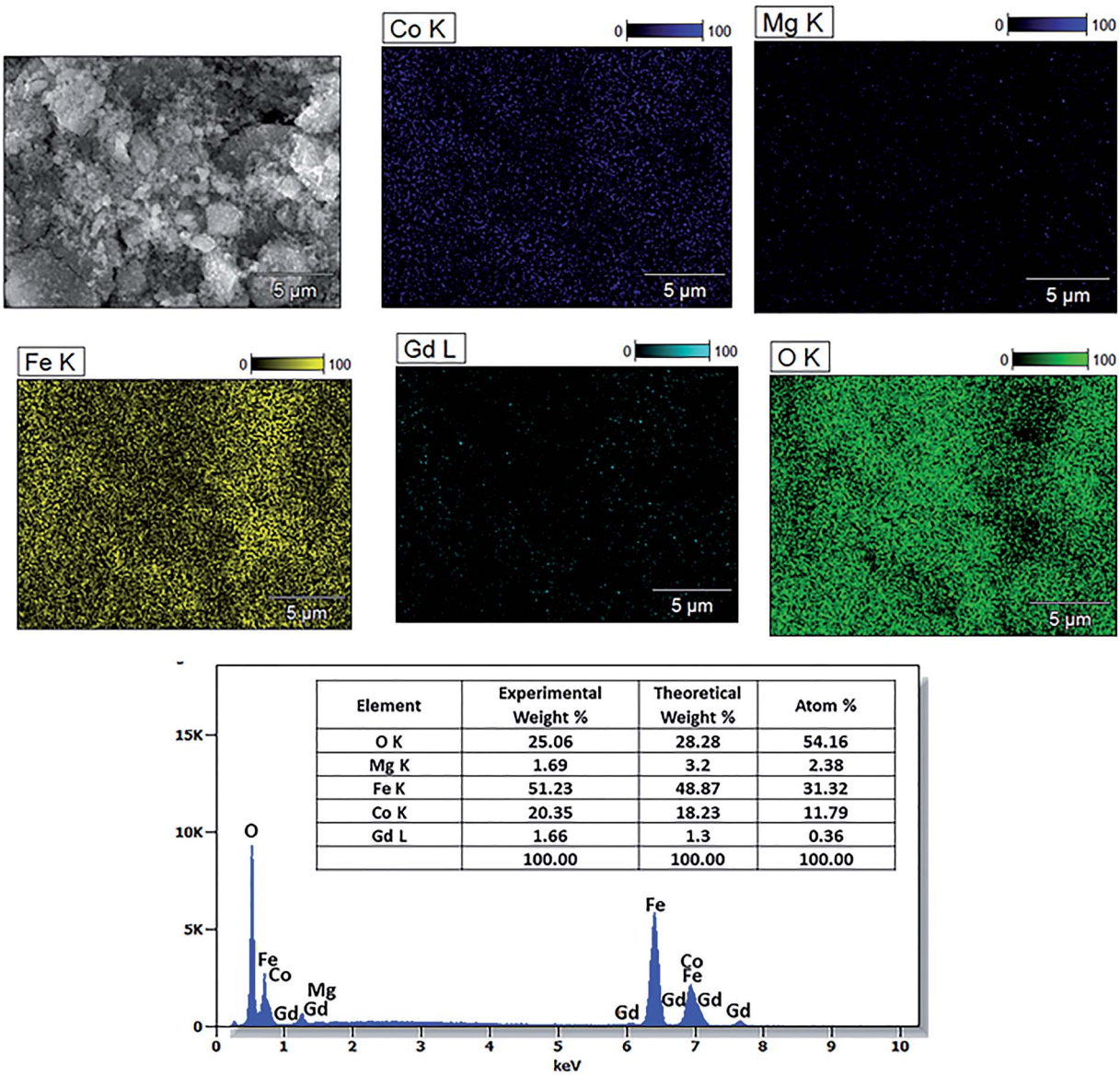

Fig. 6 EDS spectrum and elemental maps of $Co_{0.7}Mg_{0.3}Fe_{1.98}Gd_{0.02}O_4$ and the corresponding elemental composition.

$Co_{0.7}Mg_{0.3}Fe_{1.98}Gd_{0.02}O_4$. The absorption band ν_1 is assigned to the stretching vibration mode of metal–oxygen at tetrahedral sites, whereas ν_2 is attributed to octahedral sites. The positions of the two strong bands are clearly related to the difference in the Fe–O bond lengths at the A- and B-sites. The presence of the band ν_3 in $Co_{0.7}Mg_{0.3}Fe_{1.98}Gd_{0.02}O_4$ is related to the stretching vibration of the nitrate group (NO_3).[43]

Compared to $CoFe_2O_4$, the FTIR bands of $Co_{0.7}Mg_{0.3}Fe_{1.98}Gd_{0.02}O_4$ are shifted toward higher frequency, as indicated in the inset of Fig. 4 (ν_1 = 437–445 cm^{-1} and ν_2 = 749–812 cm^{-1}). These shifts are explained by the changes in the bond strength, bond length, and broadening of the tetrahedral and octahedral sites.[44]

The changes in the octahedral site were greater than those in the tetrahedral site after doping with gadolinium. Thus, it can be concluded that the gadolinium ions have a greater effect on the octahedral sites. The doping ions can increase the absorption band length of the tetrahedral and octahedral site lattice.

Table 5 Results of magnetic measurements

	M_s (emu g^{-1})	M_r (emu g^{-1})	H_c (Oe)	M_r/M_s	n_B (μ_B)	$K \times 10^5$ (erg cm^{-3})
300 K	95.68	39.99	1702.28	0.41	3.87	1.69
10 K	109.53	82.58	11 959.53	0.75	4.43	13.64

Table 6 Magnetic properties of pure $CoFe_2O_4$ prepared *via* coprecipitation

pH	Crystallite size (nm)	M_s (emu g^{-1})	M_r (emu g^{-1})	H_c (Oe)	$K \times 10^3$ (erg cm^{-3})	n_B (μ_B)	Reference
—	13	59.74	12.68	306.90	19.10	2.51	46
<6	38.59	73.58	41.20	568	—	3.08	47
—	16.84	61	15.25	419.00	—	—	48
12	15	75	19.3	400	—	—	49

In addition, Fe^{3+}, Co^{2+}, Mg^{2+}, and Gd^{3+} mainly occupy the B-sites in the spinel structure, inducing stress at the octahedral and tetrahedral sites. This leads to an increase in the ionic rays at both sites, leading to a change in frequency.

Morphological study

The external morphology of $Co_{0.7}Mg_{0.3}Fe_{1.98}Gd_{0.02}O_4$ was visualized by SEM (Fig. 5). The nanoparticles agglomerated due to their mutual magnetic interactions and high surface energy. The shapes of the particles appeared to be non-spherical.

The particle size distribution was analyzed using ImageJ software. The particle size at the surface was roughly estimated to be in the range of 30–70 nm for the Gd-doped ferrite sample, close to the value of D obtained by XRD analysis (Scherrer's method) for the same sample.

The elemental composition of the $Co_{0.7}Mg_{0.3}Fe_{1.98}Gd_{0.02}O_4$ nanomaterial sample was investigated by EDS and the elemental mapping is shown in Fig. 6. The EDS spectrum and elemental mapping confirm the presence of Co, Mg, Gd, Fe, and O in the synthesized nanoparticles; no other traceable impurities were detected within the resolution limit of EDS. The theoretical elemental composition x was calculated using the following formula:

$$x(\%) = z\frac{M}{M_T} \times 100,$$

where M is the molar mass of the element, M_T is the total molar mass, and z refers to the number of elements. The theoretical and experimental elemental compositions are presented in Table 6. The experimental elemental percentages agree with the theoretical values, and the crystal structure showed a homogeneous chemical composition.

Magnetic properties

The magnetic properties of $Co_{0.7}Mg_{0.3}Fe_{1.98}Gd_{0.02}O_4$ were investigated using a magnetic property measurement system. Fig. 6 shows the measured magnetic hysteresis loops at low and room temperature (10 and 300 K) under an applied external field of ±50 kOe. The loops indicate ferrimagnetic behavior.

The M_S values of the two curves were determined by fitting the high-field ($1/H \rightarrow 0$) data using the following function:[19]

$$M = M_S\left(1 - \frac{\alpha}{H}\right), \quad (7)$$

where α is a fitting constant, and H is the applied magnetic field. From the hysteresis loops, the magnetic parameters [M_S, H_c, remnant magnetization (M_r), squareness (M_r/M_S), anisotropy constant (K), and magnetic moment (n_B)] were calculated (Table 5).

The data in Table 5 show that M_S and M_r increased with decreasing temperature from 300 to 10 K for the doped sample, and these M_S and M_r values were higher than those of undoped cobalt ferrite. In contrast, the M_S values of some RE-doped ferrites were reported to be lower compared to that of bulk cobalt ferrite.[22] The M_S determined at 10 K was higher than that determined at 300 K. This can be explained by the decrease in thermal energy at low temperature, which leads to the alignment of magnetic moments parallel to the direction of the applied magnetic field, resulting in an increase in saturation.[45] The mechanism is exactly the opposite at high temperature, where the surface spins show some disordered states, weakening their response to the applied magnetic field and thus reducing magnetization. The higher values of M_S at high and low temperature are attributed to the migration of some ferric ions from the octahedral site to the tetrahedral site. This observed variation in the M_S and M_r can be understood by considering the structure of the ferrimagnetic cubic spinel. The number of octahedral sites (B-sites) is twice the number of tetrahedral sites (A-sites), and the magnetic moments on the octahedral and tetrahedral sites are antiparallel to each other, leading to a net magnetic moment $M_{(cal)} = M_B - M_A$. In addition, the increase in size can be correlated with the transformation of the multi-domain structure into a monodomain structure[40,41] upon doping the Co–Mg nano-ferrite with Gd^{3+}. At tetrahedral sites further from the proposed cation distribution, magnesium and ferric ions exhibit A–A exchange interactions; in contrast, at octahedral sites, cobalt, magnesium, ferric, and gadolinium ions exhibit B–B interactions. At tetrahedral and octahedral sites, bivalent (Co^{2+} and Mg^{2+}) and trivalent (Fe^{3+} and Gd^{3+}) metal ions exhibit superexchange A–B interactions. The superexchange A–B interactions are practically superior to the A–A and B–B interactions at the respective sites. The superexchange A–B interactions can increased upon the addition of Gd^{3+} in spinel nano-ferrite $Co_{0.7}Mg_{0.3}Fe_{1.98}Gd_{0.02}O_4$. This increase in A–B interaction implies an increase in M_S and n_B. Based on the literature, the particle size of pure cobalt ferrite synthesized *via* coprecipitation is between 10 and 30 nm, while M_S is in the range of 55–75 emu g^{-1} (Table 6). In the case of $Co_{0.7}Mg_{0.3}Fe_{1.98}Gd_{0.02}O_4$, as demonstrated by XRD analysis, the particle size is 54 nm, indicating that M_S increases with particle size.

The distances along with the angles between the ions play a crucial role in determining the magnetic exchange interactions. In general, for spinel ferrites, these binding angles and

Table 7 Expressions for determining the cation–cation (Me–Me) and cation–anion (Me–O) distances along with the bond angles

Me–Me	Me–O	Bond angle
$b = \frac{\sqrt{2}}{4}a$	$p = a\left(\frac{5}{8} - u(\bar{4}3m)\right)$	$\theta_1 = \cos^{-1}\left(\frac{p^2+q^2-c^2}{2pq}\right)$
$c = \frac{\sqrt{11}}{8}a$	$q = a\sqrt{3}\left(u(\bar{4}3m) - \frac{1}{4}\right)$	$\theta_1 = \cos^{-1}\left(\frac{p^2+r^2-e^2}{2pr}\right)$
$d = \frac{\sqrt{3}}{4}a$	$r = a\sqrt{11}\left(u(\bar{4}3m) - \frac{1}{4}\right)$	$\theta_1 = \cos^{-1}\left(\frac{2p^2-b^2}{2p^2}\right)$
$e = \frac{3\sqrt{3}}{8}a$	$s = a\sqrt{3}\left(\frac{u(\bar{4}3m)}{3} + \frac{1}{8}\right)$	$\theta_1 = \cos^{-1}\left(\frac{p^2+s^2-f^2}{2ps}\right)$
$f = \frac{\sqrt{6}}{4}a$		$\theta_1 = \cos^{-1}\left(\frac{r^2+q^2-d^2}{2rq}\right)$

inter-ionic distances greatly affect the magnetic characteristics. Thus, the inter-ionic distances between the cation and anion (Me–O; p, q, r, and s) and between the cation and cation (Me–Me; b, c, d, e, and f) as well as the bond angles (θ_1, θ_2, θ_3, θ_4, and θ_5) between the cation and cation–anion were calculated using the equations presented in Table 7.[40]

Tables 8, 9 and 11 show that doping with Mg^{2+} and Gd^{3+} caused the bond lengths between Me–O (r, q, and s) and Me–Me (b to f) to increase, while p decreased. An increase in site radius may be expected due to the replacement of smaller Fe^{3+} (0.067 nm) by larger Mg^{2+} (0.072 nm) and Gd^{3+} (0.094 nm) at octahedral sites. The ionic radius of a Gd^{3+} (0.094 nm) is large for the tetrahedral site; therefore, Gd^{3+} ions are forced to occupy octahedral sites. Similarly, Co^{2+} (0.074 nm) prefers to occupy octahedral sites because of its site preference binding energy. Fe^{3+} partially migrates from octahedral to tetrahedral sites.θ_1 and θ_2 are related to the A–B interaction, θ_3 and θ_4 are related to the B–B interaction, and θ_5 is related to the A–A interaction. The obtained inter-ionic binding angles are given in Table 11. Doping with Mg^{2+} and Gd^{3+} caused θ_1, θ_2, and θ_5 to decrease, while θ_3 and θ_4 increased. The increase in θ_5 indicates a strengthening of A–A interactions, while the increases in θ_3 and θ_4 suggest an increase in the strength of B–B exchange interactions. Thus, we can deduce that Fe^{3+}, Mg^{2+}, Gd^{3+}, and Co^{2+} ions at B sites along with Fe^{3+} and a low concentration of Mg^{2+} at A sites reinforce the superexchange interaction A–B, leading to increased saturation magnetization. This enhancement in magnetic properties is also attributed to the higher magnetic moment ($4f^7$ orbital, $S = 7/2$, $L = 0$, $J = 7/2$) and spin magnetic moment of Gd^{3+} compared to Fe^{3+} ($3d^5$) and Co^{2+} ($3d^7$, $L = 3$, $S = 3/2$, $J = 9/2$) due to strong L–S coupling. Recently, many studies have been devoted to the effects of various REE dopants on the physicochemical properties of ferrites, including Li–Ni, Ni–Zn, Mn–Zn, Mg–Cu, Cu–Zn.[50–54] In most of these studies, M_S decreased upon doping. Reports of increases in M_S upon doping with REs are much rarer. Rare earth ions generally occupy octahedral sites and have limited solubility in the spinel lattice due to their large ionic rays. However, their precise solubility in the spinel network has not been determined. It should also be noted that doping with low concentrations of REs causes M_S to increase, while high dopant concentrations cause M_S to decrease.[55] Our results are in good agreement with the theoretical studies of Hou Y. H. *et al.*,[56] who found that the net magnetic moment of $CoFe_2O_4$ increased upon doping with Gd^{3+}. Yu-Hua *et al.* also showed that the rare earth ions prefer to substitute for Fe^{3+} located at octahedral

Table 8 Calculated cation–anion (Me–O) and cation–cation (Me–Me) inter-ionic distances and bond angles in the $Co_{0.7}Mg_{0.3}Fe_{1.98}Gd_{0.02}O_4$ and $CoFe_2O_4$ samples

Parameter	b (Å)	c (Å)	d (Å)	e (Å)	f (Å)	p (Å)	q (Å)	r (Å)	s (Å)
$CoFe_2O_4$	2.9622	3.4735	3.6279	5.4419	5.1307	2.0622	1.8699	3.5807	3.6466
$Co_{0.7}Mg_{0.3}Fe_{1.98}Gd_{0.02}O_4$	2.9629	3.4743	3.6288	5.4432	5.1319	1.9912	1.9944	3.8190	3.6888

Table 9 Calculated bond angles of the $Co_{0.7}Mg_{0.3}Fe_{1.98}Gd_{0.02}O_4$ and $CoFe_2O_4$ samples

Parameter	θ_1 (°)	θ_2 (°)	θ_3 (°)	θ_4 (°)	θ_5 (°)
$CoFe_2O_4$	124.0221	148.1105	91.8114	125.6836	76.3662
$Co_{0.7}Mg_{0.3}Fe_{1.98}Gd_{0.02}O_4$	121.3193	136.7599	96.1482	126.6282	69.2622

sites, and the lattice constant of $CoFe_{1.875}RE_{0.125}O_4$ (RE = La, Ce, Pr, Nd, Eu, and Gd) decreased due to the decreasing ionic radius of the RE with increasing atomic number. The saturation magnetization of $CoFe_2O_4$ increases upon doping only with Eu and Gd because there are more unpaired 4f electrons for Eu^{3+} and Gd^{3+}. Similarly, Torkian *et al.*[55] reported that the magnetization of Gd^{3+}-doped Mn–Zn ferrite increased for Gd^{3+} substitution of up to 15%. The most significant result of this work is the production of Gd-doped Co–Mg nano-ferrites with magnetization much higher than that of bulk cobalt ferrite. To the best of our knowledge, this result has not been previously reported. Similar findings have been reported for sonochemically produced $CoFe_2O_4$ and $Zn_xCo_{(1-x)}Fe_2O_4$ synthesized using complex precursors (Table 10).

The experimental magnetic moment per formula unit (n_B of $Co_{0.7}Mg_{0.3}Fe_{1.98}Gd_{0.02}O_4$ was be calculated as follows:[61]

$$n_B = \frac{M \times M_s}{5585}, \quad (8)$$

where M is the molecular weight of the sample, and M_S is the measured saturation magnetization. The value of the magnetic moment varies from 3.87 μ_B at 300 K to 4.43 μ_B at 10 K, as shown in Table 7. This change in magnetic moment is in accordance with the variation in M_S.

According to the proposed cation distribution $(Mg_{0.1}Fe_{0.9})^A[Co_{0.7}Mg_{0.2}Fe_{1.08}Gd_{0.02}]^BO_4$ and using the magnetic moment values of Mg^{2+} (0 μ_B), Fe^{3+} (5 μ_B), Gd^{3+} (7 μ_B), and Co^{2+} (3 μ_B), the net magnetic moment $M_{(cal)}$ was calculated as $M_{(cal)} = M_B - M_A$, where M_A and M_B represent the net magnetic moments of lattice sites A and B, respectively. The calculated value of $M_{(cal)}$ is 3.14 μ_B, comparable with the determined experimental value. Further from the proposed cation distribution, at tetrahedral locations, magnesium and ferric ions exhibit A–A exchange interactions; in contrast, at octahedral sites, cobalt, magnesium, ferric, and gadolinium ions exhibit B–B interactions. At tetrahedral and octahedral sites, the metal ions (Mg^{2+} and Fe^{3+}) exhibit superexchange A–B interactions with Co^{2+}, Mg^{2+}, Fe^{3+}, and Gd^{3+}. Superexchange A–B interactions are practically superior to A–A and B–B interactions at the respective sites. There may be an increase in A–B superexchange interactions with the addition of Gd^{3+} to $Co_{0.7}Mg_{0.3}Fe_{1.98}Gd_{0.02}O_4$ spinel nano-ferrites. This increase in A–B interaction suggests an increase in the measured values of saturation magnetization and magnetic moment. In this work, M_S and n_B increased upon the addition of Gd^{3+} in $Co_{0.7}Mg_{0.3}Fe_{1.98}Gd_{0.02}O_4$ ferrite spinels. This increase in magnetic parameters can be correlated with the bonding angles. The bonding angles θ_1, θ_2, and θ_5 decreased upon doping, suggesting decreased A–A interactions. Meanwhile, θ_3 and θ_4 increased, indicating an increase in B–B and A–B interactions. The complete solubility of large Gd^{3+} ions at B sites could be responsible for the change in the magnetic behavior of the $Co_{0.7}Mg_{0.3}Fe_{1.98}Gd_{0.02}O_4$ nano-ferrites. This is probably why high M_S and n_B values have been obtained with low concentrations of gadolinium. For ferrites doped with high concentrations of other REs, the decrease in saturation magnetization and magnetic moment can be interpreted based on the migration of rare earth ions to the grain boundaries, resulting in weak magnetic behavior. Moreover, the magnetic parameters of spinel ferrites depend upon various factors, including the synthetic technique, sintering temperature, crystallite size, grain size, and redistribution of cations among A and B sites.

The effective anisotropy constant K can be calculated using the relationship[62]

$$H_C = \frac{K_{eff} \times 0.96}{M_s}, \quad (9)$$

where H_C is the coercivity, and M_S is the saturation magnetization. The coercivity value of the sample at 300 K is given in Table 5. It can be observed from Tables 5 and 6 show that the coercivity of the sample at 300 K was higher than that of pure cobalt ferrite synthesized *via* coprecipitation. The observed variation in coercivity can be explained as follows. As discussed above, compared to other ions, Co^{2+} exhibits stronger *L–S* coupling and a weaker crystal field, resulting in stronger magneto-crystalline anisotropy related to the increase in the concentration of high-spin Co^{2+} ions at octahedral sites.[63] Although Gd^{3+} has zero orbital angular momentum, gadolinium has been reported to contribute to and strengthen anisotropy.[64]

The coercivity of the sample increased from 1702.28 Oe at 300 K to 11 959.53 Oe at 10 K. The enhanced coercivity is attributed to the reduced thermal fluctuation energy at 10 K, which is less effective in reducing the effects of magneto-crystalline anisotropy energy. In addition, the enhanced coercivity could be interpreted as a result of the energy barriers in the nanoparticles becoming more apparent at low temperature. While these barriers always exist, they have been suggested to

Table 10 Magnetic properties of cobalt ferrite prepared by different synthetic methods

Compound	Method of synthesis	M_S (emu g^{-1} at 300 K)	M_s (emu g^{-1} at 5 K)	H_C (Oe at 300 K)	H_C (Oe at 5 K)	M_r/M_s (300 K)	M_r/M_s (5 K)	Reference
$Co_{0.7}Mg_{0.3}Fe_{1.98}Gd_{0.02}O_4$	Coprecipitation	95.68	109.5	1702.28	11 959.53	0.4179	0.7539	Present work
$CoFe_2O_4$	Classical ceramic method	88	—	141	—	—	—	57
$CoFe_2O_4$	—	80.8	93.9	—	25 200		—	58
$CoFe_2O_4$	Sonochemical method	92.5	—	807	—	—	—	59
$CoFe_2O_4$	Chemical complexes	92	109	—	12	—	—	60

Table 11 Configurations of ion pairs in spinel ferrites with favorable distances and angles for effective magnetic interactions in samples $Co_{0.7}Mg_{0.3}Fe_{1.98}Gd_{0.02}O_4$ and $CoFe_2O_4$

	A–B interaction	B–B interaction	A–A interaction
$CoFe_2O_4$	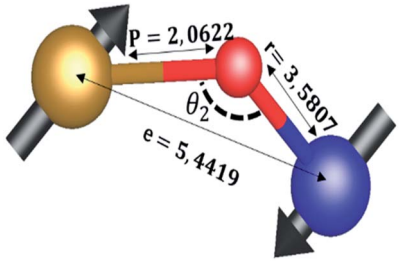	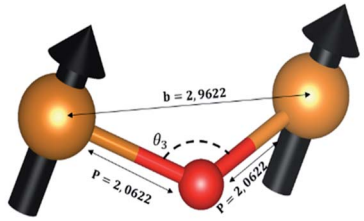	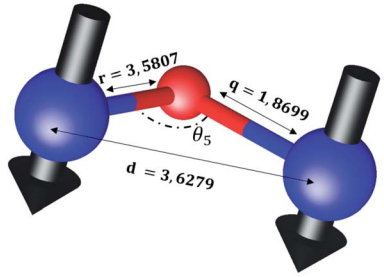
	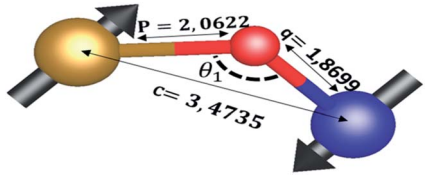	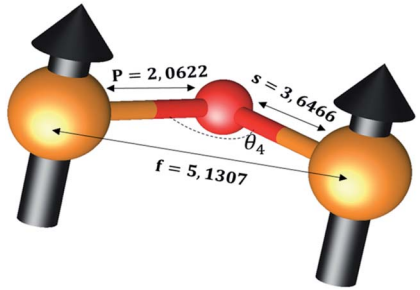	
$Co_{0.7}Mg_{0.3}Fe_{1.98}Gd_{0.02}O_4$	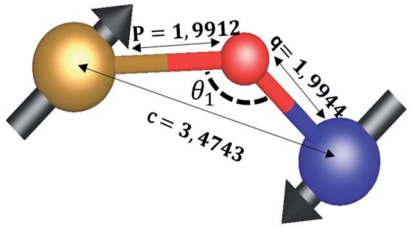	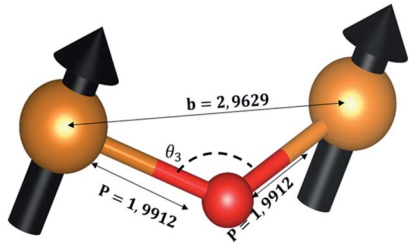	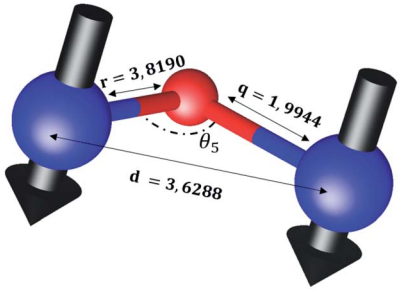
	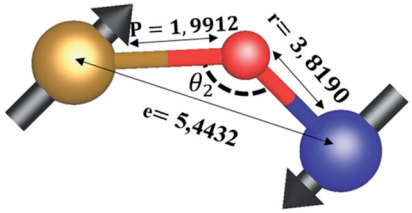	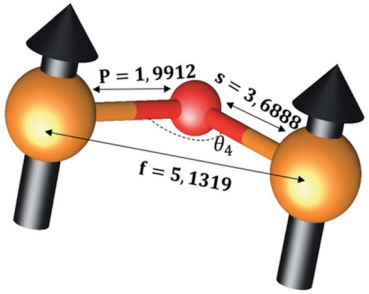	

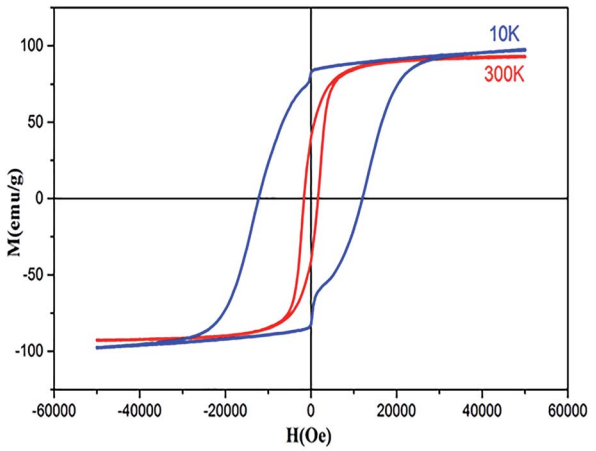

Fig. 7 Hysteresis loops of sample $Co_{0.7}Mg_{0.3}Fe_{1.98}Gd_{0.02}O_4$.

become more pronounced at low temperature; hence, these barriers might delay the alignment of magnetic moments in the direction of the applied magnetic field.

As indicated in Fig. 7, the hysteresis loops show "kink" behavior at 10 K. Various explanations have been suggested for these types of loops, including the magnetic coupling between two different magnetic phases with different coercivities. However, in this work, no secondary phase was observed. The kink behavior may also be explained by the oxidation of soft magnetic layers in the presence of atmospheric oxygen. Otherwise, this anomaly can only be attributed to the reordering of magnetic spins at 10 K under the influence of the applied field. These spin reorientations are responsible for constraining the *M–H* loop, which can be attributed to the reorientation of surface spins around particles and to the domain wall pinning of the potential wells formed by the directional order.[65]

The squareness ratio (M_r/M_S) at 300 K (0.4179) increased to 0.7539 at 10 K. At 300 K, M_r/M_S tends towards 0.5, corresponding to randomly oriented uniaxial anisotropic ferromagnetic particles. In contrast, at 10 K, M_r/M_S approaches 1, corresponding to typical isolated single-domain ferromagnetic particles. In the same vein, Stoner and Wohlfarth[66] reported that the quadratic ratio of 0.5 indicates non-interactive, randomly oriented particles that undergo coherent rotation under the effect of the applied magnetic field. For quadratic ratios below 0.5, the particles interact only through magnetostatic interactions. Exchange coupling only manifests for a quadratic ratio of higher than 0.5.

The squareness ratio obtained at 10 K confirms that we synthesized nanosized materials with high surface area; the surface effects of the magnetic nanoparticles are responsible for their uniaxial anisotropy. Kodama[67] effectively suggested that due to the high surface areas of nanomaterials, the spins at the surfaces are canted, and Néel's model of two sublattices is no longer valid. This spin canting at the surface results in higher magneto-crystalline anisotropy in nanomaterials, in good agreement with the results of this study. Such effects may be approved by the contribution from the single-ion anisotropy of Gd^{3+} in the crystal lattice in conjunction with the surface effects resulting from the alteration of the magnetic structures on the surfaces of the nanoparticles.[68]

Conclusion

In the present work, coprecipitation was found to be an economical and efficient method for the synthesis of gadolinium-doped mixed Co–Mg ferrite nanoparticles. Structural analysis indicated a single-phase cubic spinel structure of ferrite after sintering at 900 °C, while $GdFeO_3$ was observed as a secondary phase after sintering at 800 °C. The crystallite size calculated from the XRD data was in the order of 54 nm. Rietveld refinement of the XRD pattern indicated an increase in the lattice constant after doping with Gd^{3+}, which enhanced the crystallinity and induced compression deformations. The spinel structure was further confirmed by FTIR spectroscopy. EDS spectroscopy confirmed the presence of Co, Mg, Fe, Gd, and O in the investigated sample, verifying its purity and the good reactivity of gadolinium at 900 °C. The proposed cation distribution suggests that Co^{2+} and Gd^{3+} have strong preferences for the octahedral B sites, whereas Mg^{2+} and Fe^{3+} prefer to occupy tetrahedral A sites and octahedral B sites. The experimental and theoretical lattice constants were comparable. The measured saturation magnetization values at 10 and 300 K indicated that Gd^{3+} substitution in the mixed Co–Mg ferrite enhanced the saturation magnetization, which was attributed to the higher spin magnetic moment and anisotropy of Gd^{3+} compared Fe^{3+} along with the strong *L–S* coupling of Co^{2+}. Coercivity increased upon Gd^{3+} doping, which can be explained by the strong *L–S* coupling and weak crystal field of Co^{2+}, resulting in stronger magneto-crystalline anisotropy related to the increase in the concentration of high-spin Co^{2+} ions at octahedral sites. The enhancements in magnetic properties (M_S and n_B) after doping with Gd^{3+} were correlated with the changes in bond angles. Finally, we note that the obtained saturation magnetization was much higher than that of bulk cobalt ferrite.

Conflicts of interest

There are no conflicts to declare.

Acknowledgements

This research did not receive any specific grant from funding agencies in the public, commercial, or not-for-profit sectors.

References

1 P. M. Ajayan, M. Pulickel, L. S. Schadler, and P. V. Braun, *Nanocomposite science and technology*, John Wiley & Sons, 2006.
2 D. Astruc, E. Boisselier and C. Ornelas, *Chem. Rev.*, 2010, **110**, 1857–1959.
3 E. Boisselier and D. Astruc, *Chem. Soc. Rev.*, 2009, **38**, 1759.

4 C. D. Stanciu, A. V. Kimel, F. Hansteen, A. Tsukamoto, A. Itoh, A. Kirilyuk and Th. Rasing, *Phys. Rev. B: Condens. Matter Mater. Phys.*, 2006, **73**, 220402.
5 R. K. Panda and D. Behera, *J. Alloys Compd.*, 2014, **587**, 481–486.
6 A. Lakshman, P. S. V. Subba Rao and K. H. Rao, *J. Magn. Magn. Mater.*, 2004, **284**, 352–357.
7 S. K. Sharma, R. Kumar, V. V. Siva Kumar, M. Knobel, V. R. Reddy, A. Gupta and M. Singh, *Nucl. Instrum. Methods Phys. Res., Sect. B*, 2006, **248**, 37–41.
8 M. Thomas and K. C. George, *Appl. Phys.*, 2009, **47**, 6.
9 L. Wang, J. Li, W. Ding, T. Zhou, B. Liu, W. Zhong, J. Wu and Y. Du, *J. Magn. Magn. Mater.*, 1999, **207**, 111–117.
10 P. Brown and L. J. Hope-Weeks, *J. Sol-Gel Sci. Technol.*, 2009, **51**, 238–243.
11 S. L. Darshane, R. G. Deshmukh, S. S. Suryavanshi and I. S. Mulla, *J. Am. Ceram. Soc.*, 2008, **91**, 2724–2726.
12 M. K. Roy and H. C. Verma, *J. Magn. Magn. Mater.*, 2006, **306**, 98–102.
13 T. M. Clark and B. J. Evans, *IEEE Trans. Magn.*, 1997, **33**, 3745.
14 C. Liu, B. Zou, A. J. Rondinone and Z. J. Zhang, *J. Am. Chem. Soc.*, 2000, **122**, 6263–6267.
15 J.-M. Li, X.-L. Zeng and Z.-A. Xu, *Appl. Phys. Lett.*, 2013, **103**, 232410.
16 J.-M. Li, A. C. H. Huan, L. Wang, Y.-W. Du and D. Feng, *Phys. Rev. B: Condens. Matter Mater. Phys.*, 2000, **61**, 6876–6878.
17 I. Apostolova and J. M. Wesselinowa, *Solid State Commun.*, 2009, **149**, 986–990.
18 P. Kumar, J. Chand, S. Verma and M. Singh, *Int. J. Theor. Appl. Sci.*, 2011, **3**(2), 10–12.
19 Y. Mouhib, M. Belaiche and S. Briche, *Phys. Status Solidi A*, 2018, **215**, 1800469.
20 T. Prabhakaran, R. V. Mangalaraja, J. C. Denardin and J. A. Jiménez, *J. Alloys Compd.*, 2017, **716**, 171–183.
21 Q. Lin, Y. He, J. Lin, F. Yang, L. Wang and J. Dong, *J. Magn. Magn. Mater.*, 2019, **469**, 89–94.
22 Q. Lin, J. Lin, Y. He, R. Wang and J. Dong, *J. Nanomater.*, 2015, 1–6.
23 M. M. Rashad, R. M. Mohamed and H. El-Shall, *J. Mater. Process. Technol.*, 2008, **198**, 139–146.
24 L. Zhao, H. Yang, L. Yu, Y. Cui, X. Zhao, Y. Yan and S. Feng, *Phys. Lett. A*, 2004, **332**, 268–274.
25 L. Zhao, H. Yang, L. Yu, W. Sun, Y. Cui, Y. Yan and S. Feng, *Phys. Status Solidi A*, 2004, 3121–3128.
26 A. A. Sattar, A. M. Samy, R. S. El-Ezza and A. E. Eatah, *Phys. Status Solidi A*, 2002, **8**, 86–93.
27 A. Franco, F. L. A. Machado and V. S. Zapf, *J. Appl. Phys.*, 2011, **110**, 53913.
28 N. Aliyan, S. M. Mirkazemi, S. M. Masoudpanah and S. Akbari, *Appl. Phys. A*, 2017, **123**, 446.
29 S. K. Pradhan, S. Bid, M. Gateshki and V. Petkov, *Mater. Chem. Phys.*, 2005, **93**, 224–230.
30 L. Sun, R. Zhang, Q. Ni, E. Cao, W. Hao, Y. Zhang and L. Ju, *Phys. B*, 2018, **545**, 4–11.
31 D. Varshney, K. Verma and A. Kumar, *J. Mol. Struct.*, 2011, **1006**, 447–452.
32 S. Joshi, M. Kumar, S. Chhoker, A. Kumar and M. Singh, *J. Magn. Magn. Mater.*, 2017, **426**, 252–263.
33 G. P. Nethala, R. Tadi, A. V. Anupama, S. L. Shinde and V. Veeraiah, *Mater. Sci.*, 2018, **36**, 310–319.
34 N. Thomas, P. V. Jithin, V. D. Sudheesh and V. Sebastian, *Ceram. Int.*, 2017, **43**, 7305–7310.
35 N. K. Thanh, T. T. Loan, N. P. Duong, L. N. Anh, D. T. T. Nguyet, N. H. Nam, S. Soontaranon, W. Klysubun and T. D. Hien, *Phys. Status Solidi A*, 2018, **215**, 1700397.
36 F. Nakagomi, S. W. da Silva, V. K. Garg, A. C. Oliveira, P. C. Morais and A. Franco, *J. Solid State Chem.*, 2009, **182**, 2423–2429.
37 A. M. Gismelseed, K. A. Mohammed, H. M. Widatallah, A. D. Al-Rawas, M. E. Elzain and A. A. Yousif, *J. Phys.: Conf. Ser.*, 2010, **217**, 012138.
38 R. A. Pawar, S. M. Patange, A. R. Shitre, S. K. Gore, S. S. Jadhav and S. E. Shirsath, *RSC Adv.*, 2018, **8**, 25258–25267.
39 S. Panchal, S. Raghuvanshi, K. Gehlot, F. Mazaleyrat and S. N. Kane, *AIP Adv.*, 2016, **6**, 055930.
40 V. K. Lakhani, T. K. Pathak, N. H. Vasoya and K. B. Modi, *Solid State Sci.*, 2011, **13**, 539–547.
41 N. Najmoddin, A. Beitollahi, H. Kavas, S. Majid Mohseni, H. Rezaie, J. Åkerman and M. S. Toprak, *Ceram. Int.*, 2014, **40**, 3619–3625.
42 M. S. Khandekar, R. C. Kambale, J. Y. Patil, Y. D. Kolekar and S. S. Suryavanshi, *J. Alloys Compd.*, 2011, **509**, 1861–1865.
43 B. M. Ali, M. A. Siddig, Y. A. Alsabah, A. A. Elbadawi and A. I. Ahmed, *Adv. Nanoparticles*, 2018, **07**, 1.
44 H. S. Mund and B. L. Ahuja, *Mater. Res. Bull.*, 2017, **85**, 228–233.
45 S. R. Naik, A. V. Salker, S. M. Yusuf and S. S. Meena, *J. Alloys Compd.*, 2013, **566**, 54–61.
46 Z. Karimi, Y. Mohammadifar, H. Shokrollahi, Sh. K. Asl, Gh. Yousefi and L. Karimi, *J. Magn. Magn. Mater.*, 2014, **361**, 150–156.
47 A. K. Nikumbh, R. A. Pawar, D. V. Nighot, G. S. Gugale, M. D. Sangale, M. B. Khanvilkar and A. V. Nagawade, *J. Magn. Magn. Mater.*, 2014, **355**, 201–209.
48 S. Amiri and H. Shokrollahi, *J. Magn. Magn. Mater.*, 2013, **345**, 18–23.
49 R. Safi, A. Ghasemi, R. Shoja-Razavi and M. Tavousi, *J. Magn. Magn. Mater.*, 2015, **396**, 288–294.
50 M. F. Al-Hilli, S. Li and K. S. Kassim, *Mater. Sci. Eng., B*, 2009, **158**, 1–6.
51 A. C. F. M. Costa, A. P. A. Diniz, A. G. B. de Melo, R. H. G. A. Kiminami, D. R. Cornejo, A. A. Costa and L. Gama, *J. Magn. Magn. Mater.*, 2008, **320**, 742–749.
52 D. Ravinder and K. V. Kumar, *Bull. Mater. Sci.*, 2001, **24**, 505–509.
53 N. Rezlescu, E. Rezlescu, F. Tudorache and P. D. Popa, *J. Optoelectron. Adv. Mater.*, 2004, **6**, 695.
54 J. Jiang, L. Li, F. Xu and Y. Xie, *Mater. Sci. Eng., B*, 2007, **137**, 166–169.
55 S. Torkian, A. Ghasemi and R. S. Razavi, *J. Supercond. Nov. Magnetism*, 2016, **29**, 1617–1625.

56 Y. H. Hou, Y. L. Huang, S. J. Hou, S. C. Ma, Z. W. Liu and Y. F. Ouyang, *J. Magn. Magn. Mater.*, 2017, **421**, 300–305.
57 G. Dascalu, T. Popescu, M. Feder and O. F. Caltun, *J. Magn. Magn. Mater.*, 2013, **333**, 69–74.
58 M. Grigorova, H. J. Blythe, V. Blaskov, V. Rusanov, V. Petkov, V. Masheva, D. Nihtianova, Ll. M. Martinez, J. S. Muñoz and M. Mikhov, *J. Magn. Magn. Mater.*, 1998, **183**, 163–172.
59 M. Abbas, B. Parvatheeswara Rao, Md. Nazrul Islam, K. W. Kim, S. M. Naga, M. Takahashi and C. Kim, *Ceram. Int.*, 2014, **40**, 3269–3276.
60 V. Mameli, A. Musinu, A. Ardu, G. Ennas, D. Peddis, D. Niznansky, C. Sangregorio, C. Innocenti, N. T. K. Thanh and C. Cannas, *Nanoscale*, 2016, **8**, 10124–10137.
61 S. E. Shirsath, M. L. Mane, S. M. Patange, S. S. Jadhav and K. M. Jadhav, *J. Phys. Chem. C*, 2011, **115**, 20905–20912.
62 A. Nairan, M. Khan, U. Khan, M. Iqbal, S. Riaz and S. Naseem, *Nanomaterials*, 2016, **6**, 73.
63 *Modern magnetic materials: principles and applications*, ed. C. Oh. Robert and O. Handley, John Wiley Sons Inc, N. Y., 2000.
64 B. A. Calhoun and M. J. Freiser, *J. Appl. Phys.*, 1963, **34**, 1140–1145.
65 Q. Gao, G. Hong, J. Ni, W. Wang, J. Tang and J. He, *J. Appl. Phys.*, 2009, **105**, 07A516.
66 E. C. Stoner and E. P. Wohlfarth, *IEEE Trans. Magn.*, 1991, **27**, 3475–3518.
67 R. H. Kodama, *J. Magn. Magn. Mater.*, 1999, **200**, 359–372.
68 R. N. Panda, J. C. Shih and T. S. Chin, *J. Magn. Magn. Mater.*, 2003, **257**, 79–86.

